

Gaussian Process Surrogate for Shock-Ignition Plasma Simulations

(Ben Gosling - U1706745)

Multi-scale modelling techniques are widely used in physics research to help improve a simulation model by incorporating multiple models to describe a system at different scales. Such a model must incorporate the critical physics of kinetic instabilities often observed in inertial confinement fusion (ICF) experiments into large-scale fluid simulations. The significant variation in time and spatial scales between kinetic and fluid models and the computational cost of the particle in cell models have prevented the full inclusion of critical kinetic processes in ICF simulations. In this paper, we outline the possibility of using a Gaussian process (GP) surrogate model trained from shock-ignition plasma simulations to estimate key kinetic instability metrics such as laser reflectivity and hot electron temperature in order to help bridge the gap between the two competing modelling scales and reduce the computational cost of having to estimate these metrics at various intensities and plasma density-scale lengths. The GP surrogate is shown to produce the expected physics when compared to the previous work of Spencer *et. al* [1], with far less computational cost than compared to PIC simulations. Taking advantage of the inexpensive nature of the surrogate model, scaling between the threshold intensity I_{thr} and density scale length L_n was found such that $I_{thr} \propto L_n^{-0.4}$. However, further improvements to the model need to be made to allow for more accurate predictions outside the training data range. Improvements could be made by using a better approximation for the prior mean function or by tailoring better suiting kernels for the physical process that is being modelled.

I. INTRODUCTION

Shock-ignition (SI) [2, 3] is a direct inertial confinement fusion scheme [4] in which the compression and ignition phases are separated by tailoring the laser pulse profile design. In SI, the ignition phase is accomplished by modifying the typical multiple picket design of the hot-spot ignition scheme by adding a high-intensity spike pulse towards the end of the leading compression pulse as the fuel stagnates. The first stage requires a low intensity ($10^{14} - 10^{15}$ W/cm²) to ablate the outer layer of the ICF capsule, which creates a long density scale ($L_n = n_e / (dn_e/dx) \approx 300 - 1000 \mu m$) length coronal plasma and compresses the fuel [1]. The secondary stage involves high intensity ($10^{15} - 10^{16}$ W/cm²) beams to launch strong shocks into the target, which leads to a non-isobaric pressure profile throughout the capsule target. As the pressure peaks at the centre of the target, ignition occurs, and the nuclear fusion reactions become self-sustaining.

During this high-intensity phase, the average laser intensity irradiated on the target is above the threshold (i.e. $I > I_{th}$) for laser-plasma instabilities (LPI) to occur. Often these laser-plasma instabilities are three-wave parametric instabilities in which the incoming pump wave (the laser) transfers energy to two daughter waves. Examples of such instabilities are stimulated Raman scattering (SRS), stimulated Brillouin scattering (SBS) [5] and two plasmon decay (TPD) [6].

Stimulated Raman scattering is a particular instability of concern in SI concepts and is the only LPI discussed in this paper. The SRS instability transfers energy from the laser to two daughter wave modes, one being a scattered electromagnetic (EM) wave and the other an electron-plasma wave (EPW). To conserve energy and momentum, SRS is only possible in plasma regions that observe the following matching conditions for

angular frequency and wave-vector: $\omega_0 = \omega_{EPW} + \omega_s$, $\mathbf{k}_0 = \mathbf{k}_{EPW} + \mathbf{k}_s$, where the respective subscripts correspond to the laser, electron plasma wave and scattered EM wave. In this paper, we are only concerned with the case of back-scattered SRS, when the scattered EM is directly back-scattered, and the EPW is forward-scattered.

The generation of these two new modes harms the SI process's success; for example, the scattered EM wave will divert energy away from the target, reducing laser-illumination uniformity [7]. However, it is not just the scattered mode that causes issues; the EPW will transfer energy to the electrons with velocities $v \sim v_\phi = \omega/k > v_{th}$, often known as Landau damping, leading to the generation of hot-electron populations. Hot-electrons with energies greater than 100 keV are more likely to deposit their energy ahead of the shock generated from the high-intensity laser pulse [8]. The pre-heating of the fuel is disadvantageous as it significantly reduces the maximum compression that can be achieved, which diminishes the likelihood of ignition being reached.

Like with most areas of physics, experiments can be costly to run, so employing the use of computer simulations help to determine the optimal experimental setups. ICF capsule implosions are often simulated using Radiation-Hydrodynamic models. Such models use the laws of fluid mechanics to observe the evolution of the bulk plasma/material over time; to predict the achieved fuel compression and energy gain for a particular target and laser profile design. Hydrodynamic models often operate at larger time and spatial scales than the triggered kinetic scale instabilities such as SRS, which makes their effects unable to be included. However, as discussed throughout this introduction, kinetic scale instabilities can create damaging effects that are deleterious to ICF experiments. Therefore, a suitable model is required to bridge the gap between the two physical scales to include the lost kinetic physics within the large-

scale fluid simulations. The primary aim of this study is to explore the possibility of using Gaussian process (GP) regression techniques to build a suitable surrogate model from kinetic scale particle-in-cell simulations of varying laser intensity and density scale length. Such a model would help bridge the gap of escaped knowledge between the two modelling scales and drastically reduce the computational expense of kinetic modelling.

The particle-in-cell code EPOCH [9] was used to model initial plasma conditions similar to those observed in SI-relevant experiments. The simulations are all restricted to 1D to observe SRS via kinetic inflation [1] in isolation from other LPI; for example, TPD can only occur in higher spatial dimensions to conserve momenta.

The outline of this paper is as follows: Section II discusses the Gaussian process methodology and PIC simulation set-up used. Section III discusses the choice of surrogate metrics used to train the GP surrogate and how they are extracted from PIC simulations. Then the remaining sections present the key results from the GP model for a 1D (I only) and 2D input parameter space (I, L_n).

II. METHODOLOGY

A. Gaussian Process Regression

The physics of kinetic scale instabilities is lost in large-scale fluid simulations of typical ICF implosions due to the significant differences in time and spatial scales between the kinetic and fluid models. There is also a sizeable associated cost of the kinetic modelling, so a cheap surrogate model is required to help bridge the gap between the two scales. In this paper, the particle in cell code EPOCH is used to simulate a 1D LPI problem to generate a data set to train a Gaussian process (GP) surrogate model for select LPI metrics (see Sec. III).

Our underlying model is based around some function f that we would like to infer from Gaussian process regression so that we can make predictions at non-simulated locations. A GP provides a prior over functions, such that f is represented as a vector \mathbf{f} drawn from a multivariate normal with zero mean and covariance matrix \mathbf{K} :

$$f \sim \mathcal{GP} \rightarrow \mathbf{f} \sim \mathcal{N}(\mathbf{0}, \mathbf{K}). \quad (1)$$

The noisy simulation data can then be used to condition the prior distribution, such that for a given training set $\mathcal{D} = \{(\mathbf{x}_i, y_i)\}_{i=1}^N$, the outputs are taken to be:

$$y_i = f(\mathbf{x}_i) + \epsilon_i; \quad \epsilon_i \sim \mathcal{N}(0, \sigma_n^2). \quad (2)$$

This model above requires further adaptation, however, as it assumes homoscedasticity, i.e. that the noise variance is the same across the input domain. However, this is not the case, as later it is shown that there is far more certainty on the outputs than predicted from

a homoscedastic regression model. To combat this, a heteroscedastic nature was adopted, in which re-runs of the training set were performed to estimate the expected noise variance, such that our training set is based around a mean observation and its associated variance $\mathcal{D} = \{(\mathbf{x}_i, \bar{y}_i, \sigma_{n,i}^2)\}_{i=1}^N$. The prior distribution is now conditioned using the following model to account for the heteroscedastic nature:

$$y_i = f(\mathbf{x}_i) + \epsilon_i; \quad \epsilon_i | \mathbf{x}_i \sim \mathcal{N}(0, \sigma_{n,i}^2). \quad (3)$$

Assuming additive independence, then for our N noisy observations at inputs $\mathbf{X} = [\mathbf{x}_1, \dots, \mathbf{x}_N]$, the covariance matrix Σ for the observations is augmented to $\Sigma[\mathbf{y}] = \mathbf{K}(\mathbf{X}, \mathbf{X}) + \mathbf{D}$, where $\mathbf{D} = \text{diag}(\sigma_n^2(\mathbf{X}))$. One can now make predictions at new locations $\mathbf{X}^* = [\mathbf{x}^*_1, \dots, \mathbf{x}^*_M]$ giving new function values $\mathbf{f}^* = [f(\mathbf{x}^*_1), \dots, f(\mathbf{x}^*_M)]$ described via the Gaussian distribution:

$$\begin{bmatrix} \mathbf{y} \\ \mathbf{f}^* \end{bmatrix} \sim \mathcal{N} \left(\mathbf{0}, \begin{bmatrix} \underbrace{\mathbf{K}(\mathbf{X}, \mathbf{X}) + \mathbf{D}}_{\mathbf{K}} & \underbrace{\mathbf{K}(\mathbf{X}, \mathbf{X}^*)}_{\mathbf{k}_*} \\ \underbrace{\mathbf{K}(\mathbf{X}^*, \mathbf{X})}_{\mathbf{k}_*^T} & \underbrace{\mathbf{K}(\mathbf{X}^*, \mathbf{X}^*)}_{\mathbf{K}^*} \end{bmatrix} \right). \quad (4)$$

Finally, applying this result to obtain the conditional distribution $\mathbf{f}^* | \mathbf{y}$, we find that the posterior distribution for \mathbf{f}^* is a Gaussian with mean and covariance given by:

$$\mathbb{E}[\mathbf{f}^*] = \mathbf{k}_*^T [\mathbf{K} + \mathbf{D}]^{-1} \mathbf{y} \quad (5)$$

$$\Sigma[\mathbf{f}^*] = \mathbf{K}^* - \mathbf{k}_*^T [\mathbf{K} + \mathbf{D}]^{-1} \mathbf{k}_*. \quad (6)$$

To account for the heteroscedastic noise nature of the problem, the covariance matrix must be augmented to include this noise as done earlier by adding the term $\mathbf{D}^* = \text{diag}(\sigma_n^2(\mathbf{X}^*))$. However, unlike before, we no longer know the noise variance at the new locations; thus, a further model is required. Using the already known sample of variances from our sample set \mathcal{D} . The noise variance at each location is taken to behave similarly as f , i.e. as a Gaussian process, with a training set $\mathcal{D} = \{(\mathbf{x}_i, \sigma_{n,i}^2)\}_{i=1}^N$. However, this time with zero noise variance, it is assumed that the simulation/sample set is exact. The accuracy of this model, therefore, increases with the number of runs of the sample set \mathcal{D} as you tend toward the true variance of the quantity of interest at each input \mathbf{x}_i .

The choice of covariance function (kernel) is crucial to how the GP will ultimately behave, so it is wise to try and fit a kernel to the modelling problem. For the noise GP, the covariance function is taken to be that of the exponential covariance function:

$$k(\mathbf{x}, \mathbf{x}') = \sigma_f^2 \exp \left(- \sum_{h=0}^d \frac{\|\mathbf{x}_h - \mathbf{x}'_h\|_{\mathbf{L}_2}}{l_h} \right), \quad (7)$$

where d is the dimension of input \mathbf{x} and \mathbf{x}_h is the h -th dimension of input variable $\mathbf{x} \in \mathbb{R}^d$. The hyper-parameters

l_h and σ_f^2 represent the characteristic length-scale corresponding to the h -th dimension of the input \mathbf{x} and the variance term that is considered as an output-scale amplitude, respectively. This kernel was chosen as the noise is expected to vary in a non-smooth manner which is inherently random in certain regions without any form of a trend. Whereas for the output GP, we expect to see more of an underlying trend which we would like to make smoother predictions, which is why the rational quadratic kernel was chosen for the 1D input GP:

$$k(\mathbf{x}, \mathbf{x}') = \sigma_f^2 \left(1 + \sum_{h=0}^d \frac{\|\mathbf{x}_h - \mathbf{x}'_h\|_{L_2}^2}{2\alpha l_h} \right)^{-\alpha}, \quad \alpha = 2(8)$$

GP priors with this kernel are expected to see functions that vary smoothly compared to the exponential kernel. The parameter α determines the relative weighting of large-scale and small-scale variations. However, for the 2D input GP, the exponential kernel was used as, given the relatively small data set collected compared to the 1D case, the rational quadratic kernel would lead to more oscillatory predictions in the high-intensity region, which is known not to be the case. With a larger training sample, this issue could be remedied.

The tuning of these hyper-parameters is done via an optimisation routine, where the hyper-parameters $\Theta = [\sigma_f^2, l_1, \dots, l_d]$, are chosen to be those that minimise the negative marginal log-likelihood $\mathcal{L}(\Theta)$. Using the formal definition of a Gaussian distribution, $\mathcal{L}(\Theta)$ is taken to be:

$$\mathcal{L}(\Theta) = \frac{1}{2} \mathbf{y}^T [\mathbf{K} + \mathbf{D}]^{-1} \mathbf{y} - \frac{1}{2} \log |\mathbf{K} + \mathbf{D}| - \frac{N}{2} \log 2\pi. \quad (9)$$

The noise covariance matrix (\mathbf{D}) is set to null for the noise variance GP problem.

B. Simulation Set-Up

All laser-plasma simulations are performed using the particle-in-cell (PIC) code EPOCH for 1D. The initial conditions were chosen to match the set-up used in Spencer et. al, in order to compare the results of the surrogate model, as there is minimal experimental data to compare any results. All simulations used a fixed domain size of 100 microns split into 6500 evenly spaced grid cells and ran for a total period of 2 pico-seconds, with a fixed number of macro-particles corresponding to 2048 per cell. Ion dynamics and collisions are ignored as the overall simulation period is significantly less than any average time scale in which these processes operate. Thus the simulations are simplified, only simulating a collisionless electron plasma.

Absorbing boundaries are used for the electromagnetic fields (E , B), and any particles exiting the simulation are replaced with an incoming particle defined with a velocity consistent with a Maxwellian plasma based on

the initial set temperature. The background temperature was set to 4.5 keV which is consistent with most SI simulations/experiments [10, 11]. The initial particle distribution is generated using a pseudo-random number generator, so each simulation was performed several times (5 for the 1D input GP case and 3 for the 2D GP input case) to determine the sensitivity noise of the measured quantities due to plasma fluctuations.

An exponential plasma density profile is assumed such that $n(x) = n_{min} \exp(x/L_n)$, where the density scale length L_n is defined as the $n_e/(dn_e/dx)$, evaluated at the middle of the density profile n_{mid} . Shock ignition experiments have detected SRS scattered light from a density range of 0.09 - 0.16 n_{cr} [12], where the critical density n_{cr} is defined as the region where the electron plasma oscillates at the same frequency as the laser. Given this, n_{mid} was constrained to always be $0.15n_{cr}$, with the minimum and maximum densities determined from the fixed spatial and density scale lengths.

The two variables subject to change were the laser intensity I_L and density scale length L_n , which form the input basis for the GP surrogate. A training range of $10^{14} - 10^{16}$ W/cm² was chosen for I_L and 300-1000 microns for L_n as these match most SI experiments. Finally, for the case of the 1D input model, only the laser intensity is set to change, with a density scale length fixed at 500 microns.

III. SURROGATE METRICS

In order to quantify the underlying physics of LPI within our simulations, suitable metrics were derived. Inflationary SRS is expected to be observed, so it was wise to tailor the metrics to this process. SRS leads to the generation of a scattered electromagnetic wave and an electron plasma wave (EPW). Thus the metrics are formed around these two generated modes.

A. Reflectivity - \mathcal{P}

The scattered EM wave generated from SRS is detrimental to ICF experiments as it diverts energy away from the target. Therefore a simple enough metric to use to quantify the effect of this would be to measure the reflectivity $\mathcal{P} = \langle I_{SRS} \rangle / I_L$ of the back-scattered EM wave. Here, I_{SRS} and I_L are the intensities of the back-scattered EM signal and laser signal, respectively. The intensity of the scattered EM mode is equivalent to the Poynting flux, which in 1D for a wave travelling in the x direction is $S = (E_y B_z - B_y E_z) / \mu_0$. SRS will tend to produce a scattered EM wave with the same polarisation as the incident EM mode; hence for our initialised problem (y - polarised laser), $E_z, B_y \sim 0$. To measure the reflectivity, we want to extract the average back-scattered (i.e. left travelling) energy flux over the whole duration of the simulation. The calculated Poynting flux is averaged

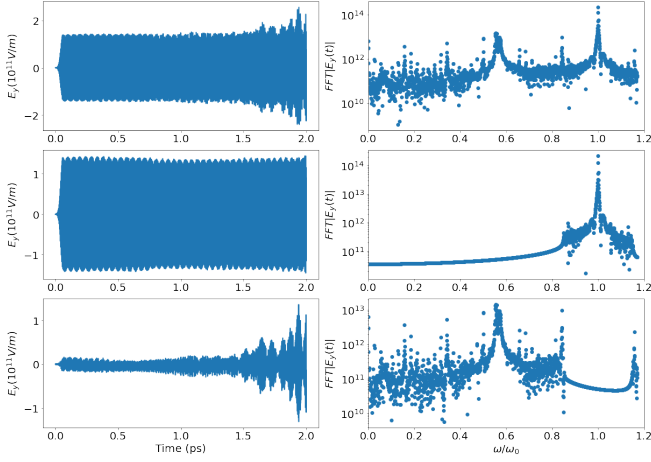


FIG. 1: Frequency filtering process used to extract the scattered SRS signal. The left-hand panels display the $E_y(t)$ field at the laser-entry boundary. The top displays the outputted signal from EPOCH, and the middle and bottom plots represent the extracted laser and SRS signal, respectively. The right-hand panels display the 1D FFT of each signal.

over all time but only close to the left-hand boundary in space (first ten cells), such that we are only estimating the back-scattered intensity,

$$\langle I_{SRS} \rangle = \frac{\sum_{i=1}^{N_x} \sum_{j=1}^{N_t} E_y^{SRS}(x_i, t_j) B_z^{SRS}(x_i, t_j)}{N_x N_t \mu_0}, \quad (10)$$

where N_x and N_t are the number of grid cells and time-steps in which we are averaging over, μ_0 is the permeability of free space, and E_y^{SRS}, B_z^{SRS} are the electric and magnetic fields of the scattered EM wave. The SRS signals are extracted using frequency filtering techniques to attain the electric and magnetic field signals corresponding to back-scattered light. SRS will tend to produce scattered light with frequencies in the range $\sim 0.5\omega_0 - 0.8\omega_0$ for the standard issue 351 nm laser beam used in ICF experiments/simulations. In order to separate scattered light from laser light, a bandpass filter was constructed centred on the laser frequency ω_0 . The band-pass filter is constructed by convolving a low-pass H^{LPF} and a high-pass filter H^{HPF} , where these low and high pass filters are windowed sinc filters h^{WS} , as the aim is to separate frequencies:

$$h_i^{WS}(\omega) = \frac{\sin(2\pi(\omega/\omega_N)(i - M/2))}{(i - M/2)} * W_{ham}(i), \quad (11)$$

$$H_i^{LPF} = \frac{h_i^{WS}(\omega = \omega_{lb})}{\sum_j h_j^{WS}(\omega = \omega_{lb})}, \quad ; \quad \omega_{lb} = 0.85\omega_0 \quad (12)$$

$$H_i^{HPF} = -\frac{h_i^{WS}(\omega = \omega_{ub})}{\sum_j h_j^{WS}(\omega = \omega_{ub})}, \quad ; \quad \omega_{ub} = 1.15\omega_0. \quad (13)$$

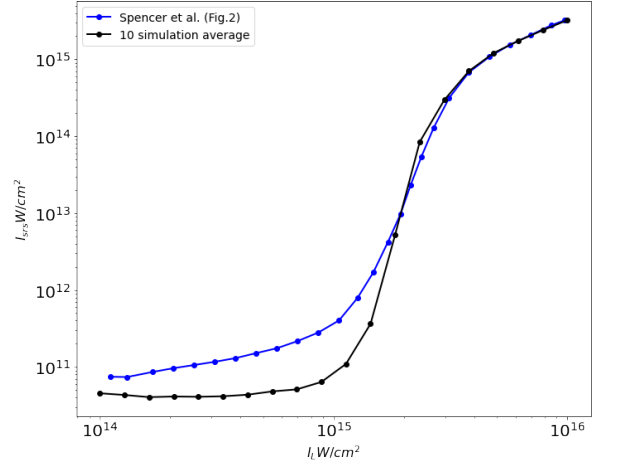


FIG. 2: Results of the measured back-scattered intensity averaged over ten simulations for the set-up used in Spencer *et. al* Fig.2.

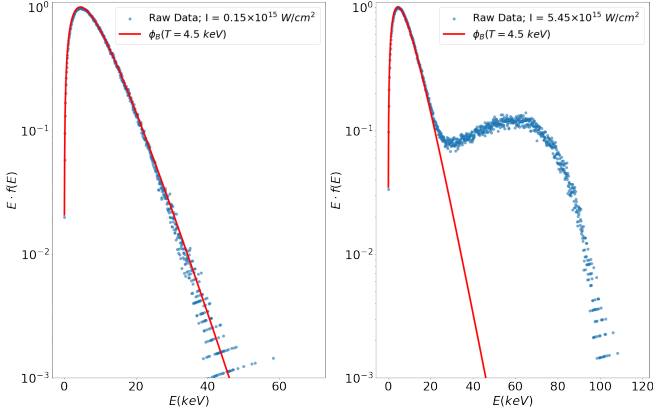
The sinc filters are convolved with a Hamming window to recover a smooth frequency response. The bandpass above is constructed to attenuate frequencies outside the frequency range $0.85\omega_0 \leq \omega \leq 1.15\omega_0$, for which we define this frequency range as that corresponding to the laser.

The laser field signals are resolved by convolving the output field $F = E_y$ or B_z , by convolving it with the band pass filter, $F^{Laser} = F * H^{BPF}$. The SRS signal can be extracted by subtracting the now known laser signal from the output field signal, i.e $F^{SRS} = F - F^{Laser}$. An example result of this frequency filtering process is shown in Fig. 1, for the E_y signal measured at the laser-entry boundary. The Fourier transform results on the right-hand side of Fig. 1 nicely shows how the laser and SRS frequency peaks are readily extracted using the technique outlined above.

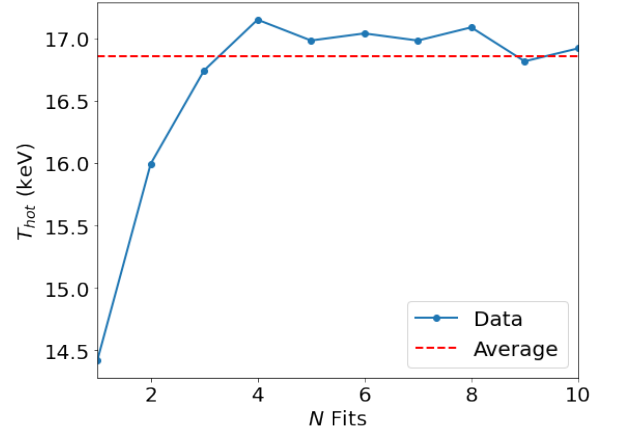
The reflectivity diagnostic was bench-marked against the results of Fig. 2 in Spencer *et. al* [1], with the bench-marking results being presented in Fig.2. The results were shown to match perfectly towards the high-intensity range; however, it was observed to be lower than the literature result in the low-intensity range. This discrepancy is likely due to the difficulty of extracting the back-scattered intensity for lower laser intensity, where we have a far more noisy Poynting flux signal as there is little to no SRS growth.

B. Hot-Electron Metrics - T_{hot}

The generation of hot electrons is another problem that arises from the presence of laser-plasma instabilities in SI experiments. These hot electrons arise due to the damping of the EPW modes generated from the SRS instability. Therefore an additional metric quantifying the severity of hot electrons for each intensity and density



(a) Energy distribution of exiting electrons, normalised by its maximum value.



(b) Hot electron temperature for an increasing number of fits.

FIG. 3: (a) Electron flux through the right-hand boundary (exit), for low-intensity and high-intensity simulation. The smooth red line corresponds to the equivalent flux for a Boltzmann distribution with $T = 4.5$ keV. (b) Observed convergence in the estimated singular hot-electron temperature with an increasing number of fits. Convergence is achieved using around five fits; thus, the number of fits chosen to measure T_{hot} was set at five.

scale length simulation was formed.

The estimated temperature of these super-thermal electron populations was chosen to quantify the severity of hot electrons within our simulation. The temperature is often found by fitting either one or many Boltzmann-like distributions to the tail end of the outgoing flux distribution. The tail-end is dominated by the population of electrons that have gained energy from the damping of the EPW. In contrast, the rest of the outputted distribution will be identical to that of a Boltzmann distribution initialised at the set background electron temperature T_e , which is observed in Fig.3a. In this paper, the fitting was done over the tail of the outgoing energy flux distribution, which we denote as $f_h(E)$ and weight it by the recorded energy, which we will label $\phi_h(E) = E \cdot f_h(E)$. The function form that was used for the fitting was:

$$\phi_B(E, T) = \frac{E \cdot \exp(-E/k_B T)}{\int_E E' \cdot \exp(-E'/k_B T) dE'}, \quad (14)$$

which matched the background electron distribution best, as shown in Fig.3a. Due to discrepancies in the measured magnitude of the raw data and Boltzmann model, all distributions are normalised against their maximum values when fitting, as we aim to fit the correct shape, which is controlled by the temperature T in ϕ_B . The hot-electron tail is extracted from the outputted distribution by finding the region where the outputted distribution function deviates from the Boltzmann curve for the background electron temperature and then smoothed using a uniform filter. Suppose the intensity is low enough to have little deviation (see Fig.3a). In that case, the entire distribution is fitted to set the hot-electron temperature to the initialised electron temperature. The observed hot-electron tail is more curved than the more

linear Boltzmann plot in Fig.3a. In reality, there are no distinct thermal species of hot-electron but several different average temperatures. Therefore to better estimate the various populations of hot-electrons produced, ϕ_h is split into n evenly spaced segments to be fitted with a Boltzmann-like distribution with some set temperature T_n . The values of T_n are chosen using a brute-force approach by finding what temperature value minimised the residual sum of squares between the raw data and the attempted Boltzmann fit.

A weighted average is performed to estimate the hot-electron temperature best. The weights are chosen to be the factor in which the magnitude of data and Boltzmann fit deviate to use as an estimate for which temperature is more populous and should therefore contribute more to the estimated average:

$$T_{hot} = \frac{\sum_n \mathcal{A}_n T_n}{\sum_n \mathcal{A}_n}; \quad \mathcal{A}_n = \frac{\text{Max}[\phi_h(\{E_n\})]}{\text{Max}[\phi_B(\{E_n\}, T_n)]}. \quad (15)$$

Increasing the number of fittings to the hot-electron tail is shown to converge towards the most likely estimate of T_{hot} , rather than using a singular fit, with the results displayed in Fig.3b showing the predicted result has converged by five fits.

IV. RESULTS AND DISCUSSION

A. 1D Input Gaussian Process

EPOCH simulations were performed for varying laser intensity at a set density scale length of 500 microns to match the density profile in Spencer et. al. A low-resolution run was first performed to test the noise model

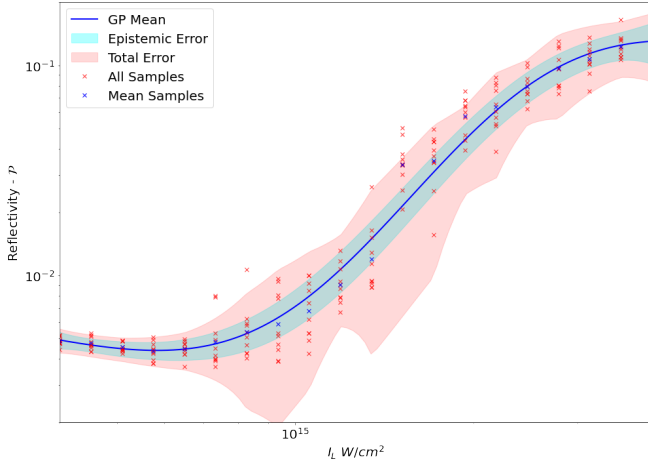


FIG. 4: Low resolution test (particle-per-cell = 100), of GP method for reflectivity (\mathcal{P}) results. The blue crosses represent the estimated mean from epoch simulations on which the GP is trained, and the red crosses are all the results from the ensemble of epoch runs. The variance found from these ensemble runs at each point is used to train the noise GP model.

and ensure that the inherent noise from plasma fluctuations is represented sensibly. The reflectivity was chosen to be the metric for this test case as the observed noise from epoch simulations was found to vary the most across the intensity space. Note that throughout this result section, the GP surrogates are trained on the log of the inputs for both metrics, as the input space range spans multiple orders of magnitude (particularly for intensity). However, only surrogate models corresponding to predicting the reflectivity are trained on the log of reflectivity data, again due to the output range spanning multiple orders of magnitude. Training on the reflectivity log also helped make the predictions more stable, as it prevented any negative predictions from being made from the GP. Training the noise model for the reflectivity required extra care as we now train on the log of the reflectivity. Thus, as the noise model is now trained on the variance of the log outputs for reflectivity, we required some relation such that the GP would output $\text{Var}[(\mathcal{P})]$ and not $\text{Var}[\log(\mathcal{P})]$. By employing the use of the Delta method, the expectation and variances of \mathcal{P} are found from the following approximations:

$$E[\mathcal{P}] \approx \exp(E[\log \mathcal{P}]), \quad (16)$$

$$\text{Var}[\mathcal{P}] \approx (E[\mathcal{P}])^2 \text{Var}[\log \mathcal{P}]. \quad (17)$$

The result displayed in Fig. 4 shows that even for a relatively small selection of points (20), the GP model can represent the reflectivity data well, with the majority of the data set (red crosses) being contained in the total 95% confidence limit. The epistemic and total error is taken to be $2\sqrt{\text{diag}(\Sigma[\mathbf{f}^*])}$ and $2\sqrt{\text{diag}(\Sigma[\mathbf{f}^*] + \text{diag}(\sigma_n^2(\mathbf{X}^*))})$, where the predicted covariance Σ is given in Eqn.6. What

is observed is that the epistemic error is found to enclose the majority of the mean points (blue crosses), which is what the GP model is trained on. However, adding the noise model helps provide a fuller picture of the variation in recorded reflectivity at each intensity location. For example, towards the lower and upper bounds of the intensity scale, the observed noise is covered reasonably well by the epistemic uncertainty. However, towards the transition region, as SRS becomes present, we observe far more significant variations in the recorded reflectivity, which is not captured by the epistemic error.

After this low-resolution test, the number of particles per cell was raised to 2048 to reduce the error from finite particle effects [1]. The resulting GP models for outputted reflectivity, hot electron temperature and hot electron abundance are shown in Fig 5. The number of intensity points was also increased to 120 points sampled using random uniform sampling, scaled to produce points within the range $10^{14} - 10^{16} \text{ W/cm}^2$. This method produces more samples towards the higher intensity range, which are of interest as SRS is likely to be present at this point, and it is this data that we would like to be included in a hydrodynamic code. All three metrics results show most of the epoch samples enclosed in the total error estimated by the GP model, suggesting that the surrogate model encapsulates the inherent randomness due to the PIC simulations. The GP surrogates match the general trend of the epoch results without over-fitting the data too much, suggesting that the optimisation process is suitable.

The predicted mean functions exhibit similar behaviour to previous works in measuring laser-plasma instabilities. Firstly, comparing the back-scattered intensity result shown in Fig.5a to that of Fig.2 in Spencer *et. al*, we see that before, the surrogate model and literature result had the same curve shape, which started to rise dramatically. The threshold intensity, which is defined as being the intensity at which this rise begins, is measured to be $1.42 \times 10^{15} \text{ W/cm}^2$ by the surrogate, which matches very well with the recorded result of $\sim 1.4 \times 10^{15} \text{ W/cm}^2$ in Spencer *et. al.*.

The average temperature of hot electrons generated by SRS has been observed in experiments to be relatively independent of intensity [13]. The hot electron temperature surrogate fits this physical trend observed in previous literature. The hot electron temperature is observed to flatten as the measure reflectively also begins to flatten.

The surrogate models can make predictions far faster than a PIC simulation. For this particle resolution and grid set-up, each PIC simulation takes around an hour to simulate. In contrast, the surrogate model, once optimised, predicts a fraction of a second. The GP mean results in Fig. 5 are for 200 logarithmic spaced intensity points, which took less than a second to predict. This almost instantaneous prediction makes a GP surrogate favourable to implement into a hydrodynamic model, as it is reasonably accurate and computationally cheap.

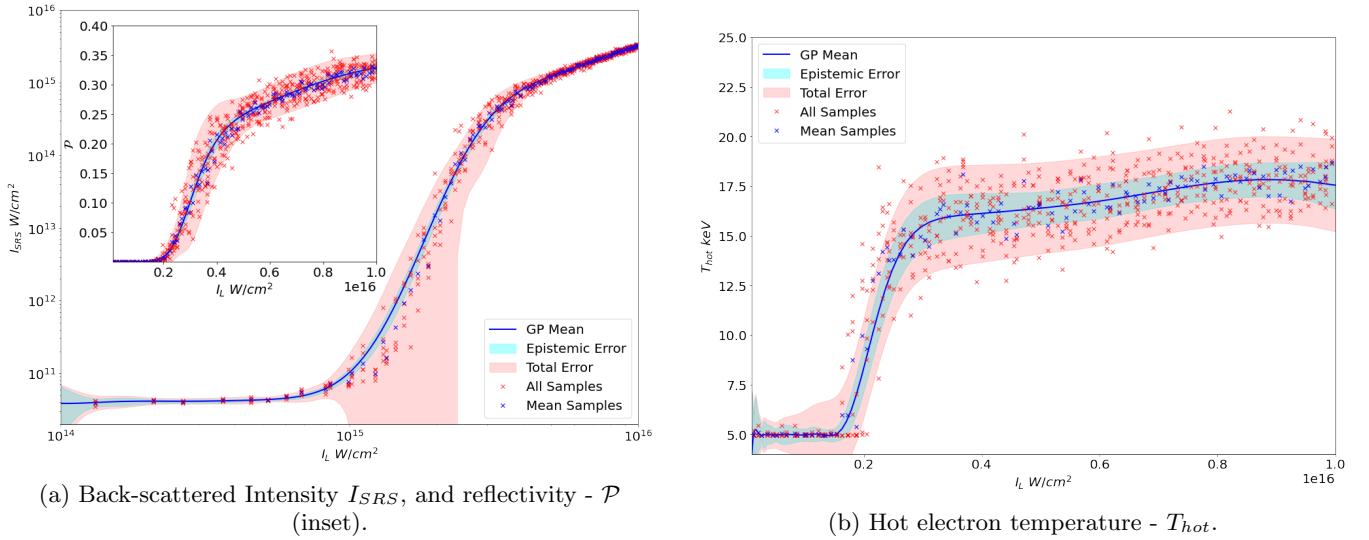


FIG. 5: Results for the 1D intensity input GP model. Insets are used for the results where the y-axis is in log-scale to better show the error outputted from the GP.

As often with GP models, extrapolating the quantity of interest outside of the training set, the estimated error begins to blow up, and the predicted mean function tends back to our prior mean estimation (zero, or in the case of log output trained models 1). Employing a better choice of mean function may help improve the extrapolation, for example, using some linear regression model [14], but the choice of the kernel also has a significant effect on how the model will behave in the extrapolated region. After observing the data X_i , the posterior mean function will be of the form:

$$m_{post}(X) = m_{prior} + \sum_i \alpha_i K(X_i, X), \quad (18)$$

for suitable α_i . Therefore having a kernel which tends to zero quickly outside the training domain will lead to poor extrapolation from the GP model. Therefore, using the rational quadratic kernel may not be best suited for extrapolating beyond the training data due to inverse square dependency on the input length scale, and perhaps using an exponential kernel would be better suited. However, given that most SI experiments operate at intensities within the training space, extrapolation is not necessarily a pressing issue. It could perhaps be more simply solved by extracting more training samples slightly beyond the upper intensity bound in this paper.

B. 2D Input Gaussian Process

It is not only the intensity that affects the presence of laser-plasma instabilities, so in this next section, we look at the results for a 2D input space, where the density scale length L_n is also varied. A collection of training samples were extracted using Latin-hypercube sampling

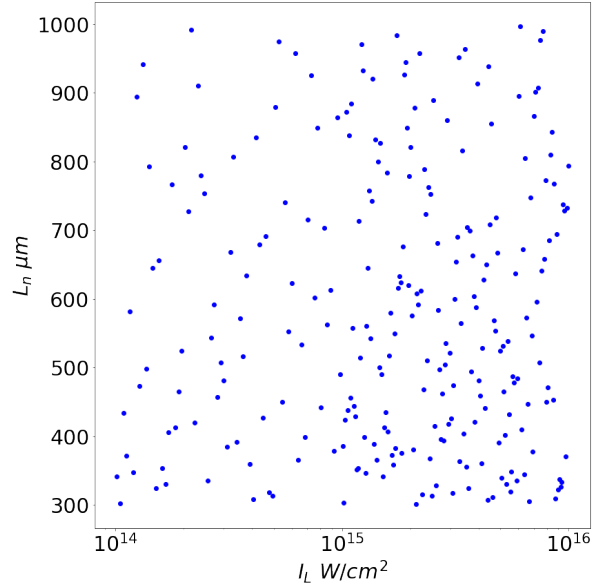


FIG. 6: Latin-hypercube samples used to train the 2D input GP model. More samples were chosen to be collected at the higher intensity range ($10^{15} - 10^{16}$ W/cm²) to predict better the effects of SRS from the limited samples that could be afforded.

to represent the input space best. To ensure that the intensity space is filled relatively evenly, the Latin hypercube sampling was done over $\log(I_L)$ rather than I_L . A total of 250 Latin-hypercube points were collected, with each point being run three times to estimate the noise from plasma fluctuations. If we used a more considerable number of runs per point, the noise variance would be better estimated. However, given the time taken to run each PIC simulation, three re-runs were chosen to

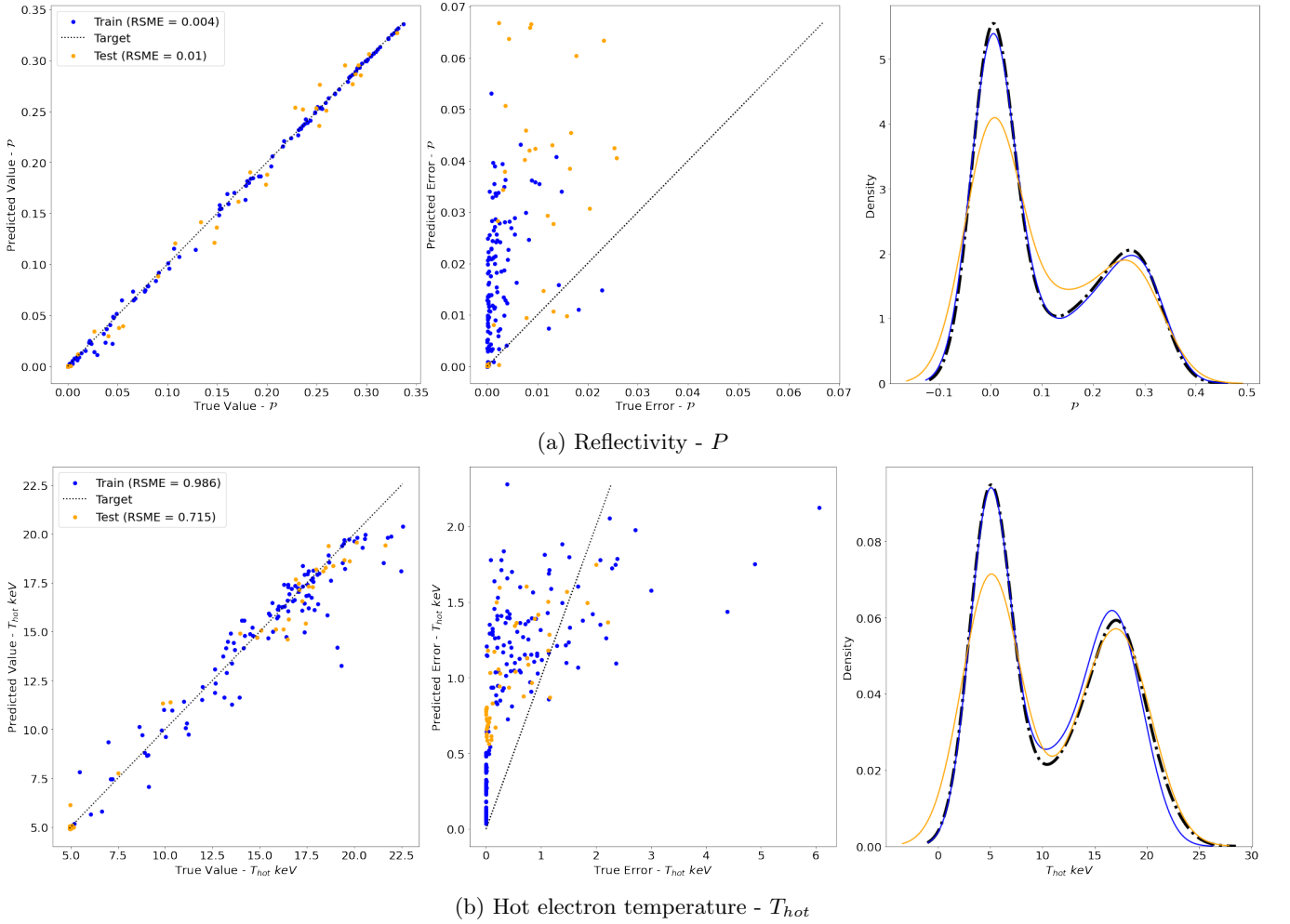


FIG. 7: Test-Train plots for the 2D GP model for the reflectivity and hot-electron temperature. The 2D GP model matches the reflectivity results well but struggles more with the hot electron temperature. This indication suggests that more fine-tuning is required to better model T_{hot} .

balance accuracy and the time taken to collect the data. Across all density scale lengths, we expect there to be little to no SRS for low initial laser intensities; hence the sampling was split into two parts. Twenty per cent of the collected Latin-hypercube points are collected between the range $10^{14} - 10^{15}$ W/cm², with the remaining eighty per cent being collected for higher intensities. This splitting was done only by a limited amount of samples that could be afforded, and the majority of SRS growth occurs at higher intensities.

Firstly, to test the performance of the GP model, test-train plots were produced (Fig.7) to observe how well the GP model did at modelling the given input data. We can see that for both metrics, the GP model matched the general trend of the data as observed in the left-hand value compare plot and the KDE plots on the right-hand side. The GP model was found to be better at matching the reflectivity data compared to the hot-electron temperature, as we see there are significantly more predicted errors being lower than the genuine error for T_{hot} than P ,

although the majority of the recorded error stay above the black dashed line.

The model then made predictions for reflectivity and hot-electron temperature for a 128×128 square grid of intensity and density scale length points to extract the predicted reflectivity and hot-electron temperature across the entire parameter space. Again, the GP surrogate was able to extract the values of P and T_{hot} at a fraction of the time, with all 16384 in 18 seconds (after hyperparameter optimisation). This is far less than performing each PIC simulation, which was found to take roughly one hour for an HPC node using 48 cores per simulation.

The resulting predictions are displayed in Fig.8, where the inset contour plots show the general trend across the input space for both LPI metrics and the prominent figure displaying the observations in intensity space. The reflectivity and temperature display the same general trend where there is an observed intensity threshold in which the reflectivity and hot-electron temperature start to grow. For the reflectivity, we find that the density scale

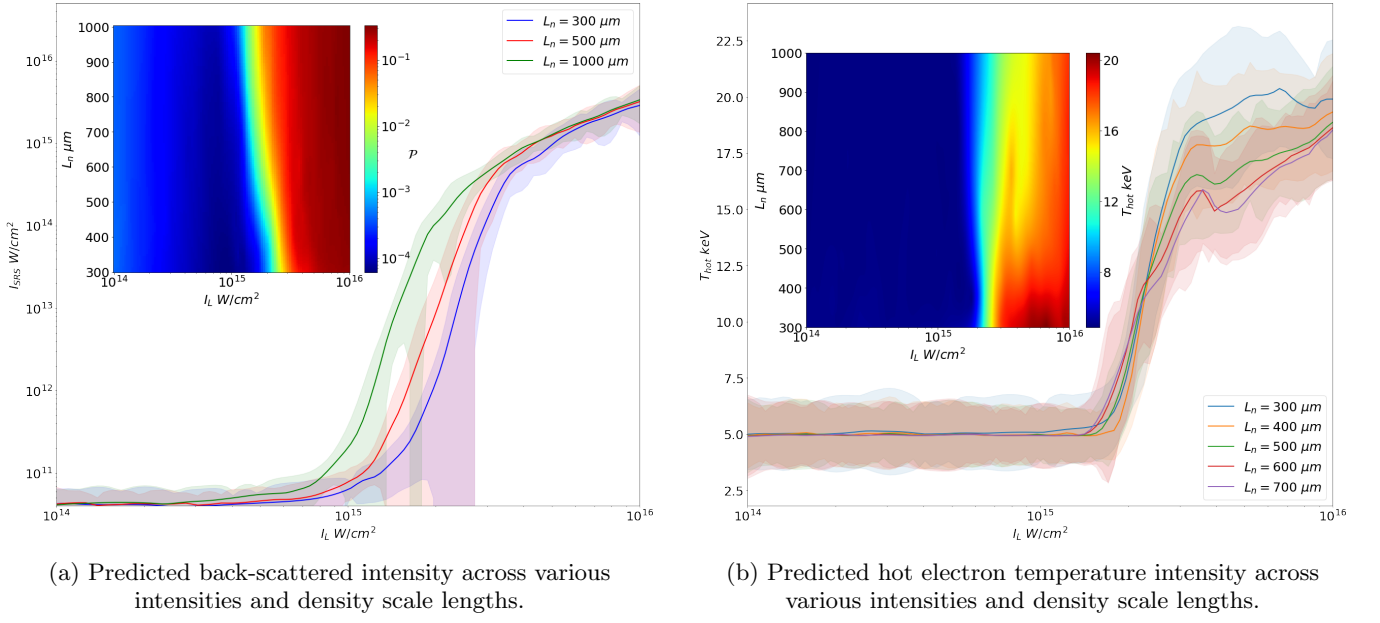


FIG. 8: Results for the 2D input GP model. Insets are used to display results across the entire sample space, with the larger figures showing the behaviour in 1D.

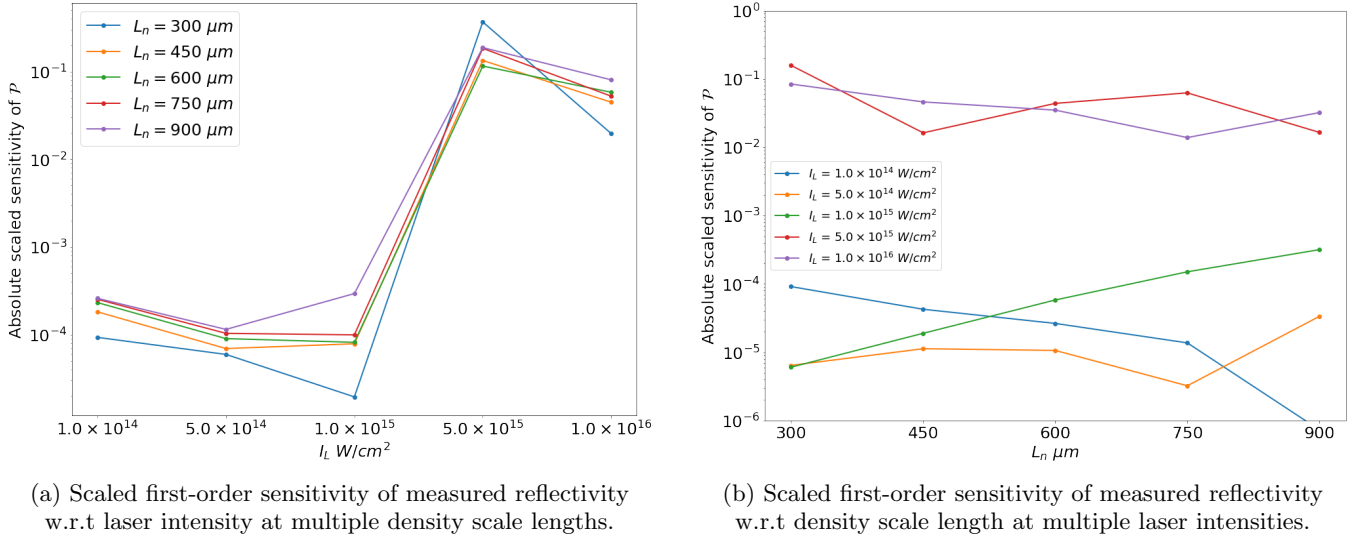


FIG. 9: First order sensitivity analysis results for measured reflectivity w.r.t each input parameter. Both results show that the measured reflectivity is far more dependent on the initialised laser intensity than the density scale length.

length has little effect on the maximum achieved reflectivity but shifts the threshold intensity, which is clearly shown by the three solid lines in Fig.8a. This physical behaviour is also shown in Fig.6a in Spencer *et al.*, in which the GP model has reproduced relatively well. Interestingly, the density scale length does appear to have more of an effect on the maximum hot-electron temperature, where it can be seen in Fig.8b, that the maximum hot electron temperature is observed to reduce a few *keV* as the density scale length increases. However, if we look back at Fig.6, it does appear that the training set is more

sparse towards the high intensity and high-density scale length region, and this effect that L_n has on the maximum achieved temperature could be due to this rather than some physical relevance.

First-order sensitivity analysis was performed to investigate how the measured reflectivity depends on the initialised intensity and density scale length. The first ordered sensitivities were calculated using a central finite difference scheme, where one input is kept constant and the other slightly changed, such that the sensitivity

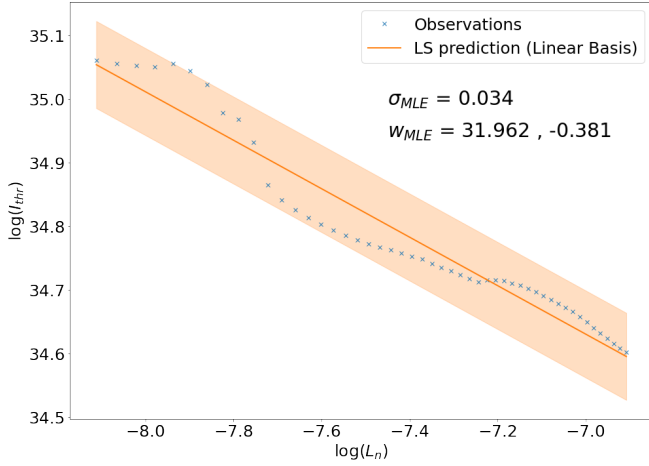


FIG. 10: Observed power law behaviour between the threshold laser intensity and density scale length. Linear regression performed on the log of the data estimated that threshold intensity has an inverse power law such that $I_{thr} \propto L_n^{-0.4}$.

is taken to be:

$$\text{Scaled Sensitivity} = \frac{\mathcal{P}((1 + \epsilon)x) - \mathcal{P}((1 - \epsilon)x)}{2\epsilon} \quad (19)$$

where x represents the changing input (either I_L, L_n) and ϵ is some small factor taken to be 1.0×10^{-6} . The GP model is used to find the reflectivity at each input as the value of \mathcal{P} can be extracted far quicker than performing multiple PIC simulations. The results from this sensitivity analysis in Fig.9 clearly show that the intensity is the dominating input parameter, particularly as the intensity becomes large enough for LPI to become more certain, with the recorded sensitivity being orders of magnitude larger.

Both the prediction and sensitivity analysis results elude an underlying relationship between the density scale length and the threshold intensity. The sensitivity analysis, as seen in Fig.9 was done over a more extensive range of intensities and density scale lengths to try and estimate the value of the threshold intensity for each density scale length which was taken to be when the measured sensitivity was found to be greater than some tolerance (set at 1.0×10^{-3}). Often, the relation between an LPI threshold intensity and the density scale length is found in the form of an inverse power law such that $I_{thr} \propto L_n^{-\alpha}$, where alpha is some real positive number [15]. Linear regression was performed on the log of I_{thr} and L_n using a linear basis set to estimate the exponent α from the gradient of the regression fit. The result displayed in Fig.10 shows a linear relation in which α is determined to be rough 0.4. Such a relation between threshold intensity and density scale length would be beneficial to implement into a hydrodynamic code, as this could be used as a proxy to see if LPI generation is present or not if one knows the laser intensity and density scale length at that point during the simulation. This

could then be used to turn on some LPI model and use the Gaussian process surrogate to estimate what temperature of hot electrons the model should initialise and how much laser energy is being reflected at that point in the hydrodynamic simulation.

V. CONCLUSION AND FURTHER WORK

To conclude, the results show that GP surrogate models can be trained to accurately match and predict the expected physics of SRS generation in one-dimensional kinetic scale models. The surrogate is found to be able to make measurements at various laser intensities and density scale lengths than general PIC simulations. However, the model at this stage depends on the amount of training data supplied as we cannot fully trust the GP predictions outside the training set, which limits the functionality of this current design. Further work will entail the development of the current model to include further inputs, such as varying input temperature and laser bandwidth, which are expected to affect the presence and severity of LPI. Attaining more PIC data to train the GP model would also significantly improve the models' predictions and lead to a better linear regression model for the threshold intensity. Furthermore, developing the current GP model is needed to find a better approximation for the prior mean function or to tailor better-suited kernels for the modelled physical process.

VI. REPRODUCIBLE RESULT

A public GitHub repository for the reproducible result is available here https://github.com/gosling123/PX915_Reproducible_Result. This repository contains a Jupyter notebook which outlines both the process of estimating the reflectivity from epoch simulations and making predictions from the GP model using the low-resolution training data displayed in Fig. 4. Validation of the measurement uncertainty is also provided by comparing the predicted standard deviation from the GP model to that from an ensemble of epoch simulations run by the notebook.

-
- [1] S. Spencer, A. Seaton, T. Goffrey, and T. Arber, Inflationary stimulated raman scattering in shock-ignition plasmas, *Phys. Plasmas* **12**, 122705 (2020).
 - [2] R. Betti *et al.*, Shock ignition of thermonuclear fuel with high areal densities, *J. Phys.: Conf. Ser.* **112**, 022024 (2008).
 - [3] L. Perkins, R. Betti, K. LaFortune, and W. Williams, Shock ignition: A new approach to high gain inertial confinement fusion on the national ignition facility, *Phys. Rev. Lett.* **103**, 045004 (2009).
 - [4] R. Craxton, K. Anderson, and T. Boehly *et al.*, Direct-drive inertial confinement fusion: A review, *Phys. Plasmas* **22**, 110501 (2015).
 - [5] C. Liu, M. Rosenbluth, and R. White, Raman and Brillouin scattering of electromagnetic waves in inhomogeneous plasmas, *Phys. Fluids* **17**, 1211 (1974).
 - [6] C. Liu and M. Rosenbluth, Parametric decay of electromagnetic waves into two plasmons and its consequences, *Phys. Fluids* **19**, 967 (1976).
 - [7] M. J. Rosenberg, A. A. Solodov, J. F. Myatt, W. Seka, P. Michel, M. Hohenberger, R. W. Short, R. Epstein, S. P. Regan, E. M. Campbell, T. Chapman, C. Goyon, J. E. Ralph, M. A. Barrios, J. D. Moody, and J. W. Bates, Origins and scaling of hot-electron preheat in ignition-scale direct-drive inertial confinement fusion experiments, *Phys. Rev. Lett.* **120**, 055001 (2018).
 - [8] D. Batani, S. Baton, A. Casner, S. Depierreux, M. Hohenberger, O. Klimo, M. Koenig, C. Labaune, X. Ribeyre, C. Rousseaux, G. Schurtz, W. Theobald, and V. Tikhonchuk, Physics issues for shock ignition, *Nuclear Fusion* **54**, 054009 (2014).
 - [9] T. Arber *et al.*, Contemporary particle-in-cell approach to laser-plasma modelling, *Plasma Phys. Control. Fusion* **57**, 113001 (2015).
 - [10] S. Baton, A. Colaïtis, C. Rousseaux, G. Boutoux, S. Brygoo, L. Jacquet, M. Koenig, D. Batani, A. Casner, E. L. Bel, D. Raffestin, A. Tentori, V. Tikhonchuk, J. Trela, C. Reverdin, L. Le-Deroff, W. Theobald, G. Cristoforetti, L. Gizzi, P. Koester, L. Labate, and K. Shigemori, Preliminary results from the Imj-petal experiment on hot electrons characterization in the context of shock ignition, *High Energy Density Phys.* **36**, 100796 (2020).
 - [11] M. J. Rosenberg, A. A. Solodov, W. Seka, R. K. Follett, J. F. Myatt, A. V. Maximov, C. Ren, S. Cao, P. Michel, M. Hohenberger, J. P. Palastro, C. Goyon, T. Chapman, J. E. Ralph, J. D. Moody, R. H. H. Scott, K. Glize, and S. P. Regan, Stimulated raman scattering mechanisms and scaling behavior in planar direct-drive experiments at the national ignition facility, *Phys. Plasmas* **27**, 042705 (2020).
 - [12] G. Cristoforetti, L. Antonelli, S. Atzeni, F. Baffigi, F. Barbato, D. Batani, G. Boutoux, A. Colaïtis, J. Dostal, R. Dudzak, L. Juha, P. Koester, A. Marocchino, D. Mancelli, P. Nicolai, O. Renner, J. J. Santos, A. Schiavi, M. M. Skoric, M. Smid, P. Straka, and L. A. Gizzi, Measurements of parametric instabilities at laser intensities relevant to strong shock generation, *Phys. Plasmas* **25**, 012702 (2018).
 - [13] R. H. H. Scott, K. Glize, L. Antonelli, M. Khan, W. Theobald, M. Wei, R. Betti, C. Stoeckl, A. G. Seaton, T. D. Arber, D. Barlow, T. Goffrey, K. Bennett, W. Garbett, S. Atzeni, A. Casner, D. Batani, C. Li, and N. Woolsey, Shock ignition laser-plasma interactions in ignition-scale plasmas, *Phys. Rev. Lett.* **127**, 065001 (2021).
 - [14] C. Rasmussen and C. Williams, *Gaussian Processes for Machine Learning* (MIT Press, 2006), doi =).
 - [15] R. K. Follett, J. G. Shaw, J. F. Myatt, C. Dorrer, D. H. Froula, and J. P. Palastro, Thresholds of absolute instabilities driven by a broadband laser, *Physics of Plasmas* **26**, 062111 (2019).